

Efficient nanorod-based amorphous silicon solar cells with advanced light trapping

Y. Kuang,^{1,2} M.C. van Lare,³ A. Polman,³ L.W. Veldhuizen,² J.K. Rath,¹ and R.E.I. Schropp^{2,4,a)}

¹*Physics of Devices, Debye Institute for Nanomaterials Science, Utrecht University, High Tech Campus, Building 21, 5656 AE Eindhoven, The Netherlands.*

²*Eindhoven University of Technology (TUE), Department of Applied Physics, Plasma & Materials Processing, P.O. Box 513, 5600 MB Eindhoven, The Netherlands.*

³*Center for Nanophotonics, FOM Institute AMOLF, Science Park 104, 1098 XG Amsterdam, The Netherlands.*

⁴*Energy research Center of the Netherlands (ECN), ECN-Solliance, High Tech Campus, Building 21, 5656 AE Eindhoven, The Netherlands.*

We present a simple, low-cost and scalable approach for the fabrication of efficient nanorod-based solar cells. Templates with arrays of self-assembled ZnO nanorods with tunable morphology are synthesized by chemical bath deposition using a low process temperature at 80°C. The nanorod templates are conformally coated with hydrogenated amorphous silicon (a-Si:H) light absorber layers of 100 nm and 200 nm thickness. An initial efficiency of up to 8.9% is achieved. External quantum efficiency (EQE) measurements on the nanorod cells show a substantial photocurrent enhancement both in the red and the blue part of the solar spectrum. Key insights in the light trapping mechanisms in these arrays are obtained via a combination of three-dimensional finite-difference time-domain simulations, optical absorption, and external quantum efficiency measurements. Front surface patterns enhance the light incoupling in the blue while rear side patterns lead to enhanced light trapping in the red. The red response in the nanorod cells is limited by absorption in the patterned Ag back contact. With these findings we develop and experimentally realize a further advanced design with patterned front and flat rear side, which shows significantly enhanced reflection from the back reflector and thus higher solar cell efficiency of 9.0%. Many of the findings in this work can serve to provide insights for further optimization of nanostructures for thin-film solar cells in a broad range of materials.

I. INTRODUCTION

Thin-film silicon is an attractive candidate in the photovoltaic (PV) market because of versatile deposition procedures, low manufacturing cost, and potential applications in flexible form. Among all the possible material structures of silicon, hydrogenated amorphous silicon (a-Si:H) is a very interesting material for single junction solar cells, as a top cell material for multiple junction solar cells such as the well-known ‘Micromorph’ concept,^{1,2} and for a-Si:H/c-Si heterojunction cells with commercially viable efficiencies of >20%.^{3,4} However, a-Si:H in thin-film solar cells suffers from a high defect density which leads to a high recombination rate. Bulk recombination is mitigated by using thinner devices, which has also added

^{a)} Author to whom correspondence should be addressed. Electronic mail: r.e.i.schropp@tue.nl.

advantages of increasing fabrication throughput and reducing light induced degradation. On the other hand, cells have to be thick enough in order to efficiently absorb the near-bandgap part of the solar spectrum. Therefore light-trapping schemes that increase optical absorption are crucial. Light scattering in thin-film solar cells is traditionally achieved by the usage of a textured transparent conductive oxide (TCO) layer, such as commercially available $\text{SnO}_2\text{:F}$ with a randomly textured surface,⁵ or textured doped ZnO fabricated either by sputtering followed by a post-deposition hydrochloric acid etching⁶⁻⁸ or by low pressure chemical vapor deposition.⁹ The textured TCO layer scatters incident light into off-normal angles to increase the light propagation path in the absorber layer. Recently radial junction solar cells based on elongated nanostructures such as nanowires,¹⁰⁻¹² nanorods,¹³⁻¹⁵ nanopillars,¹⁶⁻¹⁹ nanodomes,²⁰ and nanopyramid²¹ have attracted intense attention.

At the present stage there are several challenges to the application of elongated nanostructures in solar cells.²² One main challenge is the fabrication of large-area nanostructure arrays with controllable morphology in a cost-effective and high-throughput way. Methods such as reactive ion etching (RIE) and nanoimprint lithography that are used for the fabrication of well-defined patterns are difficult to scale up for large-area commercialization due to sample size limitations, and relatively high costs. Another main challenge is that the efficiency and the yield of these innovative solar cells based on elongated nanostructures so far are significantly lower than that for their conventional counterparts. To reach high efficiency, the very rough nanostructures must be conformally coated with device-quality absorber material, which requires smooth features. In contrast, a substrate with steep features is favorable for light scattering. So far, it has been difficult to reconcile these opposing requirements.

In our previous work we reported the application of ZnO nanorods (NRs) prepared by a lithography-free, low-cost, and scalable approach to fabricate ultrathin a-Si:H nanostructured three-dimensional (nano-3D) solar cells.^{15, 23} The nano-3D cells demonstrated a substantially enhanced photocurrent compared to flat devices as well as to randomly textured devices with similar or even larger absorber layer thickness because of efficient light trapping. However, the main challenge in this 3D concept is to achieve high open circuit voltage (V_{oc}), fill factor (FF), and yield. We found that inhomogeneous coating of the applied layers on the nanorods, especially on the side walls, leads to the generation of voids or porous regions which are detrimental to the electrical properties. Incomplete coating of the NRs leads to shunting of the front and back contacts, which is detrimental to the FF. To address these challenges, in the present work we demonstrate an advanced solar cell geometry using the ZnO nanorod scaffold with moderate aspect ratio grown on flat ZnO/Ag back contact. The new system reaches a good balance between the optical and electrical performance, maintaining the advantage of advanced light trapping, indicated by the short-circuit current density (J_{sc}), while demonstrating similar V_{oc} and FF as cells deposited on planar substrates. We measure the absorption, reflection and external quantum efficiency (EQE) spectra of the nanostructured cells and compare

these to three-dimensional finite-difference time-domain (3D FDTD) simulations that are used to study the light trapping mechanisms in more detail. The inexpensive and scalable synthetic method together with the key findings on the light trapping mechanisms for the nanostructured solar cells present in this work could be applied to many other types of thin-film solar cells.

II. EXPERIMENTAL

A. ZnO nanorod synthesis

Prior to the growth of ZnO NRs, a flat ZnO thin film seed layer was deposited onto glass (Corning Eagle XG) at room temperature via radio frequency (RF) magnetron sputtering from a ceramic ZnO target. Zinc acetate dehydrate ($\text{Zn}(\text{CH}_3\text{COO})_2 \cdot 2\text{H}_2\text{O}$, Sigma-Aldrich) with an equal molar ratio of hexamethylenetetramine (HMT, Sigma-Aldrich) was dissolved in de-ionized water to obtain a precursor solution, followed by magnetron stirring for ~15 minutes at room temperature. Synthesis of ZnO nanorods on the pre-coated glass was carried out at 80°C during a certain time, holding the seed layer side facing down in the precursor solution. The as-grown ZnO nanorods were characterized with scanning electron microscopy (SEM).

B. Solar cell fabrication and characterization

A ~200 nm thick silver layer was first deposited over the NR arrays via thermal evaporation, followed by a ~80 nm thick ZnO:Al (AZO) layer made by RF magnetron sputtering from a ZnO:2wt.%Al₂O₃ target. Deposition of an n₁-n₂-i-p (bottom to top) layer stack (nominal thickness: n₁: ~5 nm (μc-Si:H), n₂: ~25 nm (a-Si:H), i: ~100 or 200 nm (a-Si:H), p: ~15 nm (μc-Si:H)) was carried out by plasma-enhanced chemical vapor deposition (PECVD) using a radio frequency of 13.56 MHz in a multi-chamber deposition system. The deposition rate for the intrinsic layer was around 0.2 nm/s. SiH₄ was utilized for deposition of the a-Si:H n- and i-layers, while a SiH₄/H₂ mixture was employed for deposition of the μc-Si:H n- and p-layers. B(CH₃)₃ and PH₃ gases were additionally introduced for p- and n-doping, respectively. The n-i-p stack on the NR arrays was sputter-coated with 4 mm×4 mm squares of indium tin oxide (ITO) (80 nm thick). Gold top-grid contacts were evaporated onto the square ITO pads, leaving an active cell area of 0.13 cm² for each cell. Planar solar cells on Corning Eagle XG glass were fabricated as reference, simultaneously with the structured ones. Current density-voltage (J-V) measurements were performed using a Wacom dual-beam solar simulator calibrated to the AM1.5G spectrum (100 mW/cm²). To avoid carrier collection from outside the cell area, J-V measurements were performed with a thin stainless steel shadow mask with a 4 mm×4 mm opening. The EQE under short circuit condition was also investigated using a lamp in combination with a

monochromator. Reflection and transmission spectra of the completed cells were measured by a Perkin Elmer Lambda 2S double-beam spectrophotometer equipped with an integrating sphere.

C. Finite-difference time-domain simulations

Three-dimensional finite-difference time-domain (FDTD) simulations, performed using Lumerical FDTD software, were used to model the absorption in the solar cells. The full device stack, consisting of 200 nm Ag, 80 nm ZnO, 100 or 200 nm intrinsic a-Si:H and 80 nm ITO in thickness, was used in the modeling. The thin n- and p-layers were neglected in the simulations. The roughness of the back of the device was implemented in the simulation by directly importing the surface topography of the Ag coated NR substrate measured by atomic force microscopy (AFM). The roughness profile at the AZO/a-Si:H interface was assumed to be the same as that at the Ag/AZO interface. AFM scans show that the topography at the ITO/air interface was significantly smoother compared to that of the Ag-coated NR substrates. In the simulations the surface profile (ITO/air interface) was generated by taking the AFM topography of the Ag coated substrate as a starting point and smoothing it by using a combination of image dilation and Gaussian blur in Matlab. Table 1 shows the root mean square (RMS) roughness of the AFM measured topography for the Ag-coated NR substrate and for the full NR/Ag/ZnO/a-Si:H/ITO layer stack. AFM topographies were measured over a $10\ \mu\text{m}\times 10\ \mu\text{m}$ area at five different positions on the sample. The RMS roughness of the top profiles that were generated by smoothing the measured Ag profiles is also shown in Table I. The roughness profile at the a-Si:H/ITO interface was assumed to be the same as that at the ITO/air interface. In the simulations, a unit cell size of $2\ \mu\text{m}\times 2\ \mu\text{m}$ was used in combination with periodic boundary conditions. No effects of periodicity were observed for this size (no significant difference in absorption was observed when the simulation volume was increased to $2.2\ \mu\text{m}\times 2.2\ \mu\text{m}$). At the top and bottom of the simulation volume perfectly matched layers were used as boundary conditions. A uniform mesh of 5 nm was used over the whole 3D simulation volume.

TABLE I. RMS roughness of the measured AFM surface profiles for the Ag-coated NR substrate and for the full NR/Ag/ZnO/Al/a-Si:H/ITO layer stack (100 nm and 200 nm a-Si:H), and of the smoothed profiles generated from the experimental roughness of the Ag coated NR substrate.

	Ag coated NR substrate	Full stack (100 nm a-Si:H)	Full stack (200 nm a-Si:H)
Measured (nm)	81.3±1.8	58.2±5.2	47.6±2.7
Generated (nm)	-	56	49

III. RESULTS AND DISCUSSIONS

Figure 1 shows SEM images of the ZnO nanorods grown on the ZnO seed layers with thicknesses of 100 nm (a), 500 nm (b), and 1000 nm (c). For the thinner seed layer a larger site density of smaller NRs is obtained. For the 500 nm and 1000 nm

thick seed layers, well-developed crystalline NRs are obtained. We attribute the difference in NR site density to the difference in grain size at the top surface of the seed layers. A smaller grain size of the seed layer leads to a larger site density of nucleation sites and thus a higher site density of NRs with smaller diameter. The sputtered ZnO seed layer is a polycrystalline material with a preferential c-axis orientation as determined by X-ray diffraction (not shown), favoring the vertical growth of ZnO NRs. During the sputtering process the first few layers of ZnO on glass contain tiny crystallites which act as seeds for subsequent crystal growth. Indeed the grain size in the ZnO thin film, as calculated from the full width of half maximum of the (002) peak in X-ray diffraction spectra (not shown), shows a steady increase with film thickness. Figure 1(c) and (d) compare the morphology of NRs obtained at different precursor concentrations and growth time for the same seed layer thickness. When a combination of relatively high precursor concentration and long growth time is used (Figure 1(d)), a high site density of NRs with high aspect ratio is obtained, which is attributed to the larger availability of precursor molecules.

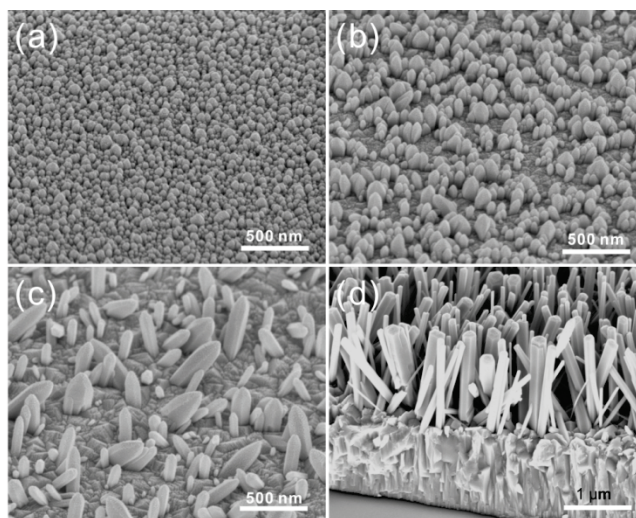


FIG. 1. SEM images (sample 45° tilted) showing the ZnO NRs prepared by chemical bath deposition. ZnO seed layers with several thicknesses were used: (a) 100 nm, (b) 500 nm, (c) 1000 nm, (d) 1000 nm. The precursor concentration and growth time for (a-c) are 0.5 mM and 1 h, while for (d) these are 10 mM and 3 hours. The growth temperature for all samples is 80°C.

For applications in solar cells, the nanostructures in Figure 1(a) are too small for efficient light scattering while the structures in Figure 1(d) are too dense for subsequent layers to fill the space between the NRs. NR arrays shown in Figure 1(c) provide a good trade-off between high aspect ratio features for light trapping and smooth enough features for a conformal coating by the device stack. This NR array is used for the devices studied in the rest of the paper.

Figure 2(a) shows a schematic diagram of the nanorod-based substrate. While in our experiments glass is employed as the mechanical carrier, metal foil or plastic could also be coated with a ZnO seed layer for the growth of NRs to fabricate

flexible solar cells. Controlling the Ag thickness is essential to control the feature size of the NR core-shell structures, which is crucial to realize conformal growth of subsequent layers. Figure 2(b) depicts an AFM image of a substrate composed of an NR array with a 200 nm thick Ag layer and an 80 nm thick ZnO:Al layer. Multiple-scale features are visible due to the random chemical growth process for the NRs. The dispersion in feature size results in a broad distribution of spatial frequencies in the scattering surface, which enables a broad spectral response.^{24, 25} Aside from acting as a buffer layer for Ag interdiffusion into the a-Si:H, the ZnO:Al layer displaces the propagating modes in the a-Si:H absorber layer from the metal back contact, which reduces the absorption in the Ag layer.²⁶ Finally, the rounded ZnO:Al features on top of the NRs can act as dielectric scatterers.^{27, 28}

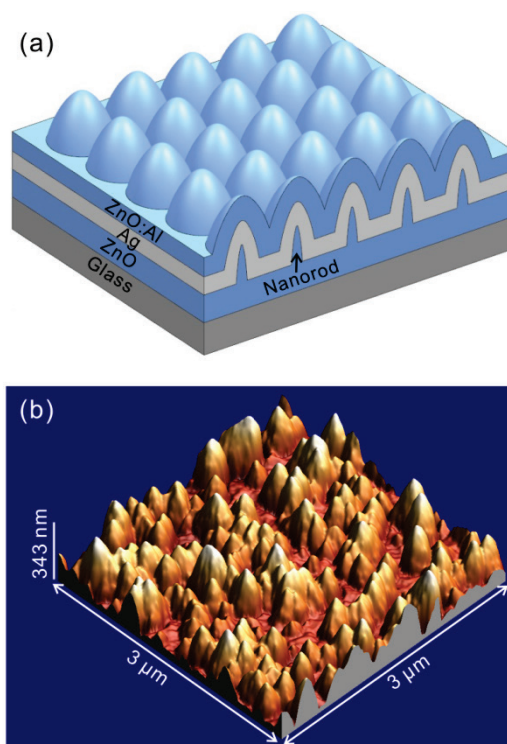


FIG. 2. Schematic diagram (a) and AFM topography (b) of the substrate with a structure of ZnO NRs/Ag/ZnO:Al.

A schematic of the full NR solar cell geometry is shown in Figure 3(a). The J-V measurements for the best cell of each type are plotted in Figure 3(b). Cell characteristics are listed in Table II. The average performance with standard deviation for the top-ten out of 42 cells with a 200 nm thick i-layer is presented in Table III, for both the NR and the flat cells. The NR cells show substantially higher efficiencies than the flat reference cells. As expected, the performance gain is in the photocurrent. The relative short-circuit photocurrent enhancements for the NR cells with respect to their flat counterparts are 46% and 30% for 100 nm and 200 nm active layer thicknesses, respectively. Strikingly, the 100 nm thick NR cell, with an

efficiency of 7.1%, outperforms the 200 nm thick flat cell, which has an efficiency of 6.4%. The best efficiency of 8.4% is achieved for the 200 nm thick NR cell, corresponding to an absolute efficiency gain of 2% with respect to its flat reference. The photocurrent gain demonstrates that the NR geometry significantly improves light trapping in the thin-film solar cells. The NR cells show a ~ 30 mV reduction in V_{oc} , with respect to the flat cells. We attribute this to the increased substrate roughness. In the present case the steep valleys between individual NRs can lead to voids and cracks in the active layer due to a shadow effect during PECVD process. In addition, in the NR cells the charge carriers experience a larger junction collection area per projected area than in the planar geometry.²⁹ The significantly enlarged interface/volume ratio in the NR system can also lead to an increased dark current. The deterioration in V_{oc} in solar cells built on elongated nanostructures has also been reported by several other groups.^{19, 20, 29–32} The reduction in V_{oc} in the NR cells obtained here is significantly less than that in our earlier work on NR cells with less homogeneous coverage of the active layer.^{15, 23} Nanostructured cells with comparable V_{oc} as planar or randomly textured counterparts have been fabricated by other researchers,^{17, 30, 33} indicating there is further room for improvement for the present nanorod geometry.

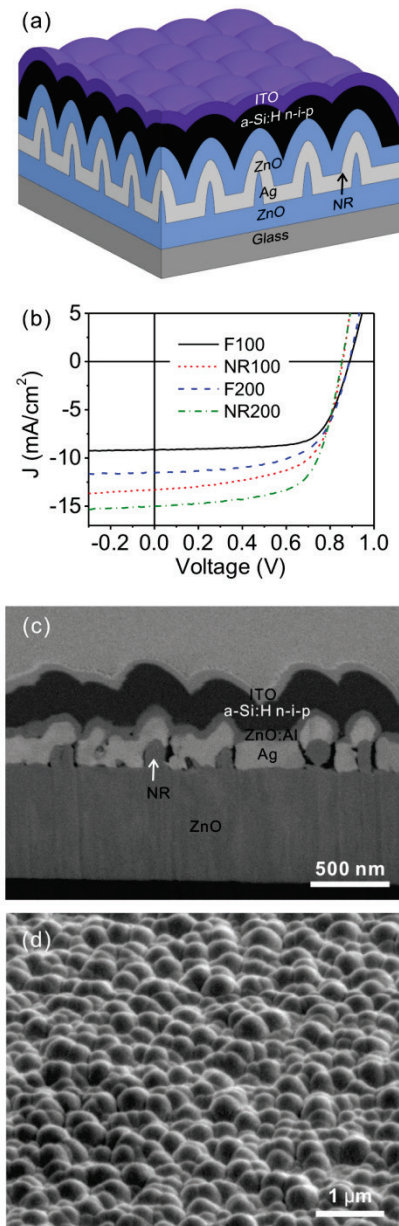


FIG. 3. Nanorod-based a-Si:H solar cells. (a) A schematic of the design. (b) J-V results of the flat (F100 and F200) and the NR cells (NR100 and NR200) with 100 nm or 200 nm thick a-Si:H absorber layers. (c) Cross-sectional view and (d) tilted (52°) top view SEM images of the completed NR cell with a 200 nm thick i-layer (NR200).

Figure 3(c) and (d) show SEM images of a cross section made by focused ion beam milling and a top view of the completed NR cell with a 200 nm thick a-Si:H i-layer. In Figure 3(c) several voids are visible between the NRs and the Ag layer. However, these defects do not propagate into the upper layers. This is in agreement with the hypothesis that the Ag and the ZnO layers smoothen the NR profile enough for growth of a high-quality absorber layer. Conformal deposition of the subsequent layers results in a corrugated top surface of the device. The corrugated surface exhibits geometrical resonances

and helps to preferentially scatter incident light into the high-index absorber layer.^{24, 27} Also the graded effective refractive index can enhance the incoupling of the incident light.³⁴

TABLE II. Characteristics of a-Si:H solar cells on NR substrates and on flat substrates, with intrinsic layer thicknesses of 100 nm and 200 nm.

Cell type	J_{sc} mA/cm ²	V_{oc} mV	FF %	Eff. %
F100	9.1	888.6	70.4	5.7
NR100	13.3	857.4	62.3	7.1
F200	11.5	886.6	62.7	6.4
NR200	15.0	853.5	65.3	8.4

TABLE III. Average of J-V parameters of the top-ten cells with 200 nm thick i-layer on the flat and the NR substrates.

Cell type	J_{sc} mA/cm ²	V_{oc} mV	FF %	Eff. %
F200	11.4±0.22	887±3	62±1	6.28±0.17
NR200	15.1±0.35	856±7	63±1	8.17±0.13

Figure 4(a) shows the absorption spectra of the whole layer stack determined from reflection and transmission measurements in an integrating sphere. The NR cells show a broadband absorption enhancement compared to their flat counterparts. The EQE for light at normal incidence in the 350-800 nm spectral range is plotted in Figure 4(b). The flat cells (F100 and F200) poorly absorb the red and infrared part of the spectrum and therefore the EQE is low in this spectral range. The NR cells (NR100 and NR200) demonstrate a broadband photocurrent enhancement and do not show the Fabry-Perot oscillations that are present in the EQE of the flat cells. In the red part of the spectrum there is a substantial photocurrent enhancement of up to 192% for the NR100 cell and 83% for the NR200 cell with respect to the flat reference cells (at ~650 nm). A strongly enhanced EQE is also observed for short wavelengths up to 500 nm, corresponding to absorption in the top region of the devices. The photocurrent enhancement in this spectral range is attributed to an enhanced incoupling of light.^{24, 27} This effect is due to geometrical (Mie) resonances of the corrugated ITO/a-Si:H surface; resonant scattering occurs preferentially into the high index absorber layer and leads to an antireflection effect. The gradual change in refractive index due to the ITO hemispherical features could also contribute to this antireflection effect. Interestingly, below ~450 nm the NR100 cell shows a higher EQE than the NR200 cell. This difference is partially due to the larger surface roughness of the NR100 cell (see Table I), leading to better light incoupling due to the resonant Mie scattering described above.

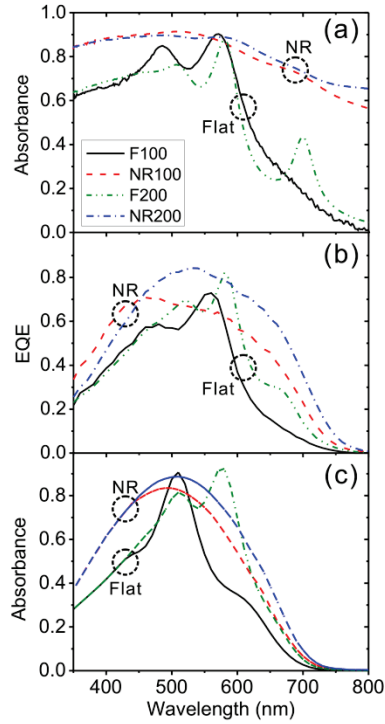


FIG. 4. Light trapping in the a-Si:H nanorod solar cells and the flat references with 100 nm and 200 nm thick i-layers. (a) Measured total absorption spectra, (b) measured external quantum efficiency spectra, and (c) simulated absorption spectra for the absorber layer.

Figure 4(c) shows the FDTD-simulated absorption in the a-Si:H layer as a function of wavelength. Similar to the trends observed in the experimental EQE spectra, both NR cells show an enhanced red and blue response compared to their flat counterparts. Unlike the EQE data, the simulated absorption curves for the two NR cells with different absorber layer thickness show a similar blue response, since the surface profiles are very similar (see Table I). Indeed, the measured absorption spectra in Figure 4(a) are very similar in the blue spectral range for the two NR cells. The difference in EQE in the blue spectral range is thus attributed to reduced carrier collection for the thicker cells.

Figure 5(a-d) shows the simulated spectra of the absorption in individual layers for the four different cell geometries as well as the reflection spectra of the devices. Several interesting trends can be observed. First of all, the absorption spectra in the intrinsic layer are quite different for the two flat cells, due to the difference in Fabry-Perot modes for the two thicknesses. These flat cells also show large reflection due to poor light trapping in the infrared. Second, the NR cells show a broadband enhanced absorption in the intrinsic layer, with the highest absorption for the thick layer, as expected. In the NR cells the reflectivity is strongly reduced over the entire spectral range, compared to the flat cells. At the same time, absorption in the Ag is substantially larger than for the flat cells for wavelengths larger than 500 nm. Third, for all cell types absorption in the ITO is a significant loss factor at wavelengths below 500 nm. This loss is slightly higher in the NR cells, which is inherent to

the resonant behavior of the dielectric structures at the top. Figure 5(e) shows the simulated electric field intensity in the different layers for incident plane waves at 670 and 720 nm wavelengths. Due to the random geometry of the layer stack a complex field distribution is observed. Strong optical hotspots are observed at the ZnO/Ag interface, consistent with the enhanced absorption in the Ag layer. Some hotspots are also observed at the ITO/air interface at positions that depend on wavelength. This demonstrates that the random nature of the pattern, with different feature sizes and hence resonances at different wavelengths, leads to a broad spectral response enhancement.

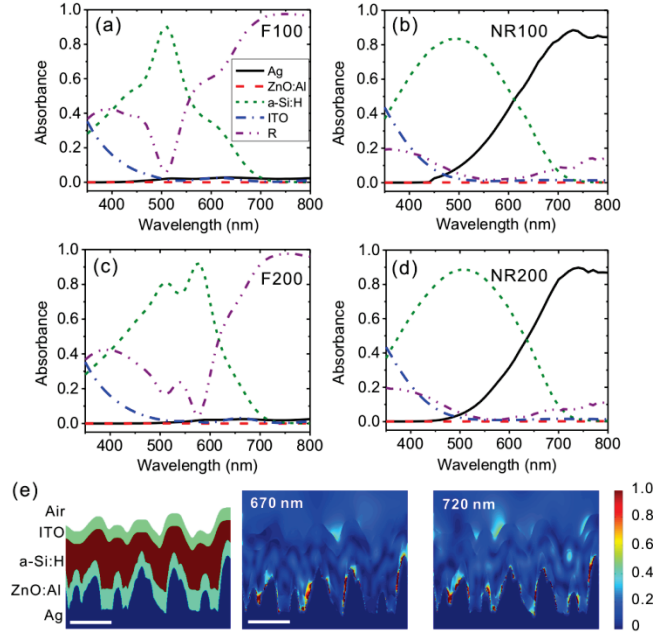


FIG. 5. FDTD simulations of the absorption spectra of individual layers for the flat (a, c) and the NR (b, d) cells with 100 and 200 nm intrinsic layer thicknesses; reflectivity (R) is also shown. (e) Cross sections of the electric field intensity at 670 nm and 720 nm for an incident plane wave for the NR200 cell. Field intensities are normalized to the incident field (color scale bar). The different layers are indicated at the left schematic. The scale bars are 500 nm.

To investigate the light scattering contribution of the rear- and the front-side nanopatterns to the optical performance of the devices, solar cells with several configurations are characterized with 3D FDTD simulations. Figure 6(a) shows the studied five geometries: 1) flat structure (Flat): all interface are flat, 2) nanorod geometry (NR): all interfaces are textured, 3) patterned-back-flat-front (Flat front): textured Ag/AZO and AZO/a-Si:H interfaces, but flat a-Si:H/ITO and ITO/air interfaces, 4) patterned-front-flat-back (Flat back): textured a-Si:H/ITO and ITO/air interfaces, but flat Ag/AZO and AZO/a-Si:H interfaces, and 5) NR on flat Ag (Flat Ag): textured AZO/a-Si:H, a-Si:H/ITO and ITO/air interfaces, and flat Ag/AZO interface. Figure 6(b) and (c) show the simulated absorption spectra in the a-Si:H layer and in the Ag layer, respectively, for these different geometries. The roughness used at the a-Si:H/ITO and ITO/air interfaces is the same as in the simulations of

the NR200 cell shown in figure 5(e), while the a-Si:H thickness used is 350 nm to enable for a constant volume of the different layers in all the geometries.

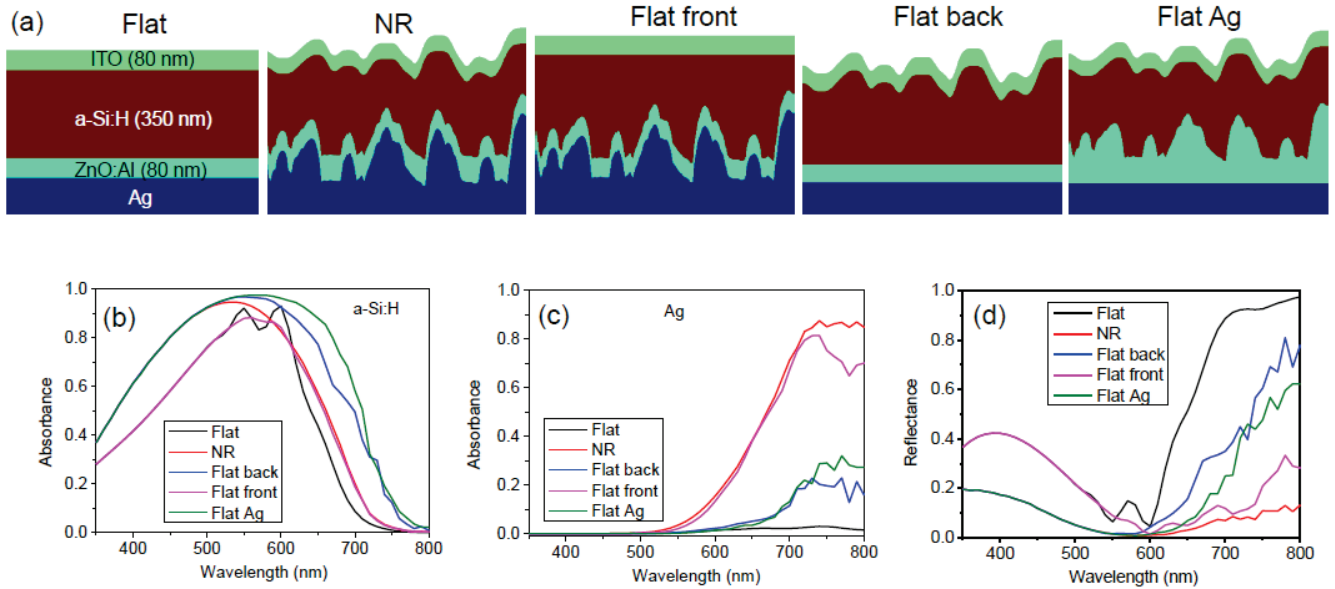


FIG. 6. Contribution of the rear- and the front-side pattern to light trapping in a-Si:H solar cells. (a) Schematic cross sections of the structures used for modeling. Simulated absorption spectra (b) in the a-Si:H layer and (c) in the Ag layer. (d) Simulated reflection spectra of the devices. The volume of the a-Si:H absorber layer is kept constant in all the geometries and is equivalent to that of a 350 nm flat intrinsic layer.

Comparing the spectra for the flat and the NR cells, the same trends are observed as described above for the F100/F200 and NR100/NR200 cells: both blue- and red-response are enhanced in the NR cells. The effect of light trapping in the infrared is relatively small in Figure 6 because of the large a-Si:H thickness (350 nm). Flattening the front surface of the NR cell reduces the absorption in the a-Si:H in the blue, confirming the importance of surface roughness for light incoupling in the blue spectral region. Indeed, the reflectance is significantly enhanced in the blue as shown in Figure 6(d). Interestingly, for this geometry also a reduced red response is observed (Figure 6(b)), indicating that light scattering from the surface topography leads to enhanced light trapping. Surprisingly, the device with rough surface and flat back (Flat back) shows the second highest absorption in a-Si:H, surpassing the counterpart with flat surface and rough back (Flat front). For the flat back geometry, the absorption in the a-Si:H in the red is significantly higher than for the standard nanorod geometry (NR). This is due to a strongly reduced absorption in the Ag, as shown in Figure 6(c). The flat Ag geometry (Flat Ag), in which all the interfaces are textured except for the Ag/AZO interface, shows the overall highest absorption in the a-Si:H absorber. Compared to the standard NR geometry, the blue response is very similar but the red response is further enhanced in the flat Ag geometry, which is mainly due to the increased reflection at the flat Ag/AZO interface, while the textured AZO/a-Si:H

interface significantly contributes to light trapping in the red region. This demonstrates that a rough Ag interface is not essential for light trapping and structuring only the upper interfaces of the device can lead to very efficient light trapping.

Figure 6(d) shows the simulated reflection for the five geometries. As expected, the geometries with flat surface (Flat and Flat front) show higher reflection in the blue than the geometries with textured surfaces. On the other hand, the reflection is significantly enhanced in the red spectral range for the geometries with flat back due to the suppressed parasitic absorption in the flat Ag layer. The device with flat Ag/AZO and textured upper interfaces (Flat Ag) shows a significantly lower reflection in the red range than that with flat Ag/AZO and AZO/a-Si:H interfaces (Flat back), which is consistent with the higher red absorption in the a-Si:H layer observed in figure 6(b) for the flat Ag geometry.

Based on these findings, solar cells with ZnO nanorods grown on a flat back reflector were made. For this design, first a 500 nm thick Ag layer was deposited on Corning glass by thermal evaporation, followed by a 1 μm thick ZnO:Al (0.5 wt.%) via magnetron sputtering as the seed layer. The growth parameters for ZnO nanorods on Ag/ZnO:Al stack are the same as those for the nanorods shown in Figure 1(c). After that a 300 nm thick ZnO:Al (2 wt.%) was deposited on the ZnO nanorods to improve both the conductivity and the surface profile for a conformal coating of the upper layers. The solar cell stack and the front contact are the same as those used for the nanorod cell shown in Figure 3(c). Standard nanorod solar cells shown in Figure 3(c) were deposited simultaneously during the thin film silicon and the ITO depositions, and are used as reference.

Figure 7 shows the experimental J-V (a) and spectral response (b) data for the flat Ag concept and the standard nanorod geometry. The absorbance ($1-R$, where R is the reflectance) of the devices is also plotted in Figure 7(b). The higher efficiency of 8.9% for the nanorod cell shown in Figure 7(a) with respect to 8.4% for the nanorod cell with an identical configuration shown in Figure 3(a) and (b) is mainly attributed to a further optimization on the p-layer, as indicated by the improved V_{oc} and fill factor. The cell with flat Ag/AZO interface demonstrates a higher current density (Figure 7(a)) and a slightly higher efficiency of 9.0% with respect to the standard NR geometry. However, the spectral response in the red is not obviously enhanced in the former. In the reflection spectra in Figure 7(b) the flat Ag geometry exhibits a significantly higher reflection in the red range, consistent with the simulated reflection in Figure 6(d). This indicates there is potential to achieve additional absorption in the active layer by increasing the a-Si:H layer thickness. Future work will focus on optimization on the thickness and band gap of the absorbing material, e.g. using a lower band gap absorbing material such as a-SiGe:H to harvest more current gain in the red, using the flat Ag geometry.

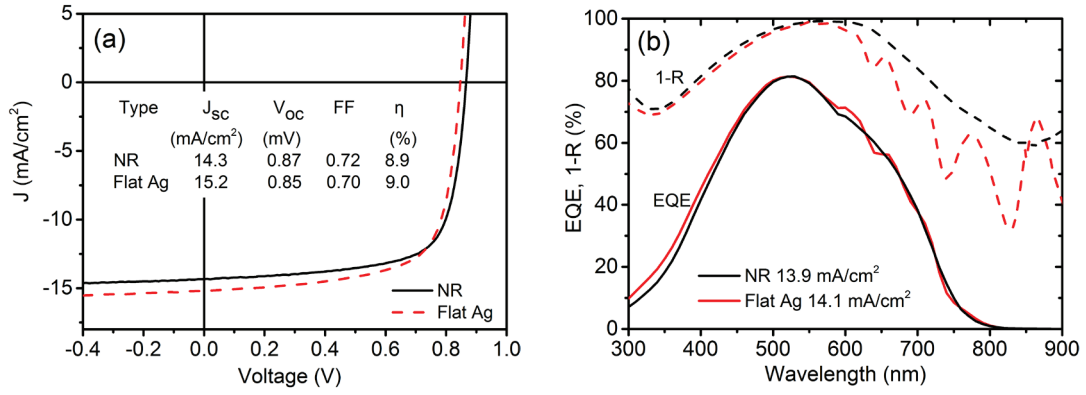


FIG. 7. J-V (a) and spectral response and absorption (b) for the solar cells based on the flat Ag geometry and the standard nanorod geometry, as schematically shown in Figure 6 (a). The nominal thickness for the intrinsic a-Si:H layer is 200 nm.

IV. CONCLUSIONS

In summary, we present an efficient nanostructured thin-film a-Si:H solar cell based on a ZnO nanorod scaffold. A ZnO nanorod array is obtained by a simple and inexpensive chemical bath deposition process at low temperature (80°C) and the morphology is tuned by adjusting seed layer thickness, reactant concentration, and growth time. EQE measurements on the NR cells show a broad enhancement with respect to the flat cells over almost the entire 350-800 nm spectral range. Corrugation at the top of the NR devices leads to an enhanced blue-response and light trapping is observed in the red part of the spectrum. 3D FDTD simulations are in good agreement with the experimental EQE measurements and show complex field profiles inside the cell. Reflection is significantly reduced for the NR cells, but absorption in the patterned Ag layer is relatively high. Our simulations show that for devices with a flat Ag/ZnO:Al interface and textured a-Si:H/ITO and ITO/air interfaces, light trapping is further enhanced due to a reduced absorption in the Ag layer. This advanced design is experimentally realized, demonstrating an enhanced photocurrent density and an initial efficiency up to 9.0% with a 200 nm thick a-Si:H absorber layer. The nanorod growth approach presented in this work does not involve complex manufacturing procedures or equipment requirements. This inexpensive design opens up a new platform for novel efficient cell design that can be made at low cost. With proper back contact material the nanorod substrate is applicable for a variety of PV systems based on e.g. multi-junction thin-film Si, CdTe, and $\text{CuIn}_x\text{Ga}_{1-x}\text{Se}_2$.

ACKNOWLEDGMENTS

Y. K. gratefully acknowledges the financial support from China Scholarship Council (CSC) under contract no. 2009615001. We thank Karine van der Werf for solar cell deposition and D. A. Matthijs de Winter for focused ion beam-

induced scanning electron microscopy. SARA Computing and Networking Services is acknowledged for support in using the Lisa Compute Cluster. This work is part of the research program of FOM, which is financially supported by NWO. This work is also supported by NanoNext, a micro-nano technology program of the Dutch Ministry of Economic Affairs and the European Research Council.

REFERENCES

- ¹A. Shah, P. Torres, R. Tscharnner, N. Wyrsh, and H. Keppner, *Science* **28**, 692 (1999).
- ²H. Keppner, J. Meier, P. Torres, D. Fischer, and A. Shah, *Appl. Phys. A* **69**,169 (1999).
- ³Y. Tsunomura, Y. Yoshimine, M. Taguchi, T. Baba, T. Kinoshita, H. Kanno, H. Sakata, E. Maruyama, and M. Tanaka, *Sol. Energy Mater. Sol. Cells* **93**, 670 (2009).
- ⁴M. Taguchi, A. Yano, S. Tohoda, K. Matsuyama, Y. Nakamura, T. Nishiwaki, K. Fujita, and E. Maruyama, *IEEE J. Photovoltaics* **4**, 96 (2014).
- ⁵<http://www.agc.com/english/csr/env/products/3.html>.
- ⁶O. Kluth, B. Rech, L. Houben, S. Wieder, G. Schöpe, C. Beneking, H. Wagner, A. Löffl, and H. W. Schock, *Thin Solid Films* **351**, 247 (1999).
- ⁷J. Müller, B. Rech, J. Springer, and M. Vanecek, *Sol. Energy* **77**, 917 (2004).
- ⁸M. Berginski, J. Hüpkes, M. Schulte, G. Schöpe, H. Stiebig, B. Rech, and M. Wuttig, *J. Appl. Phys.* **101**, 074903 (2007).
- ⁹S. Fayé, J. Steinhauser, N. Oliveira, E. Vallat-Sauvain, and C. Ballif, *Thin Solid Films* **515**, 8558 (2007).
- ¹⁰B. Tian, X. Zheng, T. J. Kempa, Y. Fang, N. Yu, G. Yu, J. Huang, and C. M. Lieber, *Nature* **449**, 885 (2007).
- ¹¹E. C. Garnett and P. Yang, *J. Am. Chem. Soc.* **130**, 9224 (2008).
- ¹²M. D. Kelzenberg, S. W. Boettcher, J. A. Petykiewicz, D. B. Turner-Evans, M. C. Putnam, E. L. Warren, J. M. Spurgeon, R. M. Briggs, N. S. Lewis, and H. A. Atwater, *Nat. Mater.* **9**, 239 (2010).
- ¹³B. M. Kayes, H. A. Atwater, and N. S. Lewis, *J. Appl. Phys.* **97**, 114302 (2005).
- ¹⁴M. Krunk, A. Katerski, T. Dedova, I. Oja Acik, and A. Mere, *Sol. Energy Mater. Sol. Cells* **92**, 1016 (2008).
- ¹⁵Y. Kuang, K. H. M. van der Werf, Z. S. Houweling, and R. E. I. Schropp, *Appl. Phys. Lett.* **98**, 113111 (2011).
- ¹⁶Z. Fan, H. Razavi, J. W. Do, A. Moriwaki, O. Ergen, Y. L. Chueh, P. W. Leu, J. C. Ho, T. Takahashi, L. A. Reichertz, S. Neale, K. Yu, M. Wu, J. W. Ager, and A. Javey, *Nat. Mater.* **8**, 648 (2009).

- ¹⁷M. J. Naughton, K. Kempa, Z. F. Ren, Y. Gao, J. Rybczynski, N. Argenti, W. Gao, Y. Wang, Y. Peng, J. R. Naughton, G. McMahon, T. Paudel, Y. C. Lan, M. J. Burns, A. Shepard, M. Clary, C. Ballif, F. Haug, T. Söderström, O. Cubero, and C. Eminian. *Phys. Status Solidi RRL* **4**, 181(2010).
- ¹⁸M. Vanecek, O. Babchenko, A. Purkrt, J. Holovsky, N. Neykova, A. Poruba, Z. Remes, J. Meier, and U. Kroll, *Appl. Phys. Lett.* **98**, 163503 (2011).
- ¹⁹J. Kim, A. J. Hong, J. W. Nah, B. Shin, F. M. Ross, and D. K. Sadana, *ACS Nano* **6**, 265 (2012).
- ²⁰J. Zhu, C. M. Hsu, Z. Yu, S. Fan, and Y. Cui, *Nano Lett.* **10**, 1979 (2010).
- ²¹A. Mavrokefalos, S. E. Han, S. Yerci, M. S. Branham, and G. Chen, *Nano Lett.* **12**, 2792 (2012).
- ²²Y. Kuang, M. Di Vece, J. K. Rath, L. van Dijk, and R. E. I. Schropp, *Rep. Prog. Phys.* **76**, 106502 (2013).
- ²³Y. Kuang, K. H. M. van der Werf, Z. S. Houweling, M. Di Vece, and R. E. I. Schropp, *J. Non-Cryst. Solids* **358**, 2209 (2012).
- ²⁴V. E. Ferry, M. A. Verschuuren, M. C. V. Lare, R. E. I. Schropp, H. A. Atwater, and A. Polman, *Nano Lett.* **11**, 4239 (2011).
- ²⁵M. Boccard, C. Battaglia, S. Hänni, K. Söderström, J. Escarré, S. Nicolay, F. Meillaud, M. Despeisse, and C. Ballif, *Nano Lett.* **12**, 1344 (2012).
- ²⁶F. J. Haug, T. Söderström, O. Cubero, V. Terrazzoni-Daudrix, and C. Ballif, *J. Appl. Phys.* **106**, 044502 (2009).
- ²⁷P. Spinelli, M. A. Verschuuren, and A. Polman, *Nat. Commun.* **3**, 692 (2012).
- ²⁸M. Van Lare, F. Lenzmann, and A. Polman, *Opt. Express* **21**, 20738 (2013).
- ²⁹J. M. Spurgeon, H. A. Atwater, and N. S. Lewis, *J. Phys. Chem. C* **112**, 6186 (2008).
- ³⁰C. M. Hsu, C. Battaglia, C. Pahud, Z. Ruan, F. J. Haug, S. Fan, C. Ballif, and Y. Cui, *Adv. Energy Mater.* **2**, 628 (2012).
- ³¹D. Kieven, T. Dittrich, A. Belaidi, J. Tornow, K. Schwarzburg, N. Allsop, and M. Lux-Steiner, *Appl. Phys. Lett.* **92**, 153107 (2008).
- ³²V. E. Ferry, M. A. Verschuuren, H. B. T. Li, R. E. I. Schropp, H. A. Atwater, and A. Polman, *Appl. Phys. Lett.* **95**, 183503 (2009).
- ³³V. E. Ferry, M. A. Verschuuren, H. B. T. Li, E. Verhagen, R. J. Walters, R. E. I. Schropp, H. A. Atwater, and A. Polman, *Opt. Express* **18**, A237 (2010).
- ³⁴G. Mariani, Z. Zhou, A. Scofield, and D. L. Huffaker, *Nano Lett.* **13**, 1632 (2013).